Solubility study of binary systems containing sulfur dioxide and water : A combination of Raman spectroscopy and Monte Carlo molecular simulation

Khouloud Saadallah, Véronique Lachet, Benoit Creton, Marie-Camille Caumon, Aurélien Randi, Jérôme Sterpenich

Solubility study of binary systems containing sulfur dioxide and water: a combination of Raman spectroscopy and Monte Carlo molecular simulation

Khouloud Saadallah[a, *], Véronique Lachet[b], Benoit Creton[b], Marie-Camille Caumon[a], Aurélien Randi[a], Jérôme Sterpenich[a]

[a]*Georessources laboratory, Université de Lorraine, CNRS, BP 70239, F-54506 Vandœuvre-lès-Nancy, France*
[b]*IFP Energies nouvelles, 1 et 4 avenue de Bois-Préau, 92852 Rueil-Malmaison, France*

Abstract

Carbon Capture, Utilization and Storage (CCUS) is one of the mitigation approaches that can be used to control CO_2 emissions into the atmosphere and to limit global warming. The CO_2 stream injected underground may contain small amounts of associated gaseous components such as SO_2. One of the key parameters needed to predict the physical and chemical evolution of the storage is solubility. Unfortunately, there is only scarce information on hazardous binary systems containing such gases. The purpose of this study is to acquire new thermodynamic data on SO_2 under geological conditions of pressure and temperature. The solubility of SO_2 in water is measured by Raman spectroscopy using high-pressure optical cells and capillary capsules after a calibration based on Monte Carlo (MC) molecular simulation and literature data. New solubility data are measured in the temperature range 20 °C–120 °C and pressures up to 25 bar. By introducing an empirical temperature-dependent or temperature-independent binary interaction coefficient k_{ij} between water and sulfur dioxide, it is possible to obtain a good agreement between experiments and MC simulations in both liquid-vapor and liquid-liquid conditions.

Keywords: CO_2 storage ; Thermodynamics ; SO_2 solubility ; Raman spectroscopy ; Molecular Simulation

1. Introduction

In the aim of facing global warming and the significant increase in Earth temperature, the net-zero commitments must be backed by valuable actions[1]. The reduction of greenhouse gas emissions into the atmosphere remains one of the important mitigation methods. The focus on CO_2 as one of the main greenhouse gases is due to long lasting of carbon dioxide into the atmosphere and the large amount of CO_2 emitted by the industry. Indeed, CO_2 remains in the atmosphere longer than other major heat-trapping gases emitted by industrial activities[2]. CO_2 capture involves the combustion of fossil resources referring to the burning of oil, natural gas, and coal to generate energy. Various technologies were proposed to regulate the anthropogenic CO_2 emissions. One of them is the carbon capture, utilization and storage (CCUS) technique[3]. In this case, CO_2 is captured from large point sources, compressed, transported and then utilized or stored into geological formations which can be saline aquifers or depleted reservoirs[4]. There are different CO_2 capture methods including post-, pre-, and oxy-combustion processes. Depending on the steam sources and the capture method used, the gas steam may include other co-captured gases. For example, the oxy-combustion capture can generate a small percentage of SO_2, N_2, Ar and O_2[5]. A complete purification of CO_2 prior to the storage is not considered in most cases because of its low efficiency, high costs and energy-consumption during the separation process[6]. The capability of storing CO_2 along with other impurities is still under research. The existence of these impurities might impact the design and operation of CCUS[7]. Indeed, CO_2 and the associated gases may react with the subsurface components including the

* Corresponding author. Tel.: +33611818901, *E-mail address:* Khouloud.saadallah@univ-lorraine.fr

reservoir rocks and the downhole well equipment. In addition, these impurities can modify the physical properties of the gas stream[8]. Besides, the presence of impurities might have an impact as well on trapping mechanisms by modifying the properties of the injected fluid and the physic-chemical conditions of trapping (redox, pH, liquid-gas equilibria …)[9].

Therefore, it is mandatory to take these co-injected gases into consideration when designing and processing the capture, transport, and storage. The knowledge of thermodynamic properties of these gas mixtures is required to understand the role played by those impurity gases in CCUS. Thermodynamic data such as solubility are required to understand and predict, based on geochemical codes[10,11], the behavior of the gases injected in subsurface geological formations.

SO_2 is one of these impurity gas. Its concentration can be up to 1.5% in the mixture [12]. Thus, its partial pressure in the mixture is never exceeding a few bar. Before moving into the study of ternary mixtures containing CO_2, SO_2 and water, the major focus is the solubility of SO_2 in water. Nowadays, this system begins to be the subject of various investigations as it is related to many industrial applications including the design of flue-gas desulfurization processes or CCUS operations[9]. SO_2 is an acidic, reactive chemical species. It has a very high solubility compared to other gases. Its solubility is about 100 times higher than CO_2 (Figure ***1***).

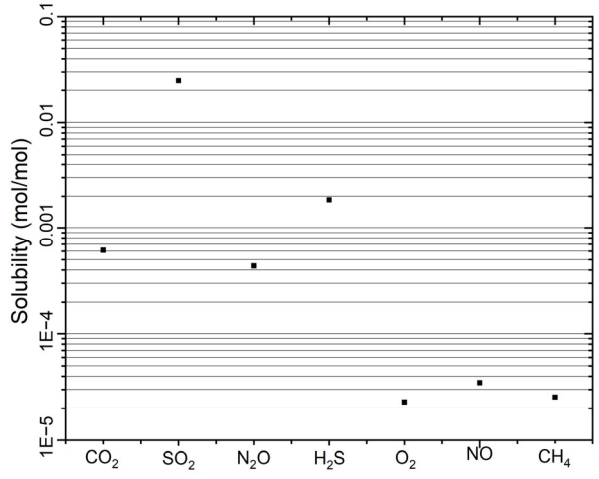

Figure 1: Solubility of some gases in water at 25 °C and 1 bar[13].

Unfortunately, only scarce information is available in the literature[14–30] for the SO_2/H_2O mixtures. Most of the studies were carried out at low pressure and temperature range as shown in Figure 2. Only few of them are performed at higher pressure[25].

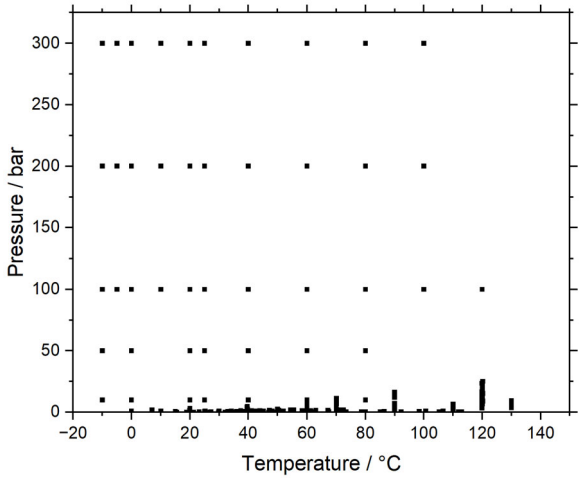

Figure 2: Pressure and temperature conditions covered by the experimental data available in the literature for SO_2 solubility in water[14–30].

The scarcity of available data might be due to the toxicity and hazardous nature of SO_2, along with some potential corrosion issues. It is known that the latter can be toxic even at low concentrations in the atmosphere. Indeed, the Occupational Exposure Limit Values are between 2 ppm (average) and 5 ppm (short term) [31]. Handling SO_2 requires special precautions when it comes to the material used to avoid corrosion.

The purpose of this study is to determine the solubility of SO_2 in water at pressure lower than 25 bar (to remain in the liquid-vapor domain) and temperature up to 80°C, in relation with CCUS conditions. In this study, experimental data using Raman spectroscopy along with the high-pressure optical cells (HPOC) and capillary capsules were conducted in a first part. The second approach was to use Monte Carlo (MC) molecular simulation technique to predict the vapor-liquid and liquid-liquid equilibria including the solubility data for SO_2/H_2O mixtures. Such simulations were performed in a previous study[32] for this binary system. However, the simulation results were not in good quantitative agreement with available experimental data. In this paper, we propose hereafter a comparison of different models used to describe H_2O and SO_2 molecules in the simulations including the use of both *T*-dependent and constant binary interaction parameters (k_{ij}). The solubility values for SO_2 in pure water experimentally determined in this study were compared with

experimental data of SO_2 solubility from literature and with MC molecular simulations from this work.

Nomenclature

CCUS	Carbon Capture, Utilization, and storage
FSCC	Fused Silica Capillary Capsule
HPOC	High Pressure Optical Cell
PAR	Peak Area Ratio
P	Pressure
T	Temperature
NPT	Isobaric-isothermal ensemble
RDSCS	Relative Differential Scattering Cross Section
MC	Monte Carlo
TIP4P	Transferable Intermolecular Potential with 4 sites
SPC	Simple Point Charge
CBMC	Configurational Bias Monte Carlo
k_{ij}	Binary Interaction Parameter

2. Materials and methodologies

2.1. High pressure optical cells

The experimental method for this study has been already used for various applications[33–37]. In this technique, both microcapillaries and *in situ* Raman measurements are combined. In this case, the capillary is considered as a micro-reactor that makes possible, using Raman spectroscopy, to study different fluid characteristics[38] including the solubility, diffusivity, and the chemical composition. Experiments were performed using pure water (deionized Milli-Q water, 18.2 MΩ.cm). The mixtures were prepared from a high purity SO_2 (99.9% purity, ALPHAGAZ^{TM}/Air Liquide).

The use of microcapillaries that have small cell volumes allows to achieve high pressure and high temperature values suitable to work under safe conditions when dealing with samples containing toxic gases such as sulfur dioxide. Samples are loaded into fused silica capillary tubing with round cross-sections with an external coating of polyimide layer (Polymicro Technologies). The outside diameter for the tubing is 354.8 µm and the internal diameter is 251.4 µm. The total length for the tubing used is 7.5 cm.

The first step is to remove the external protective layer for the tubing using a micro-torch. The purpose behind this is to get the potential for *in situ* spectroscopic analysis and for an optimized optical observation[39]. At the beginning, only one end of the tubing is being welded to load the sample from the open extremity. Water is loaded inside the capillary using a syringe (< 0.1 µL). The capillary is then glued to 1/16" outside diameter stainless steel tube using an epoxy glue which showed a better chemical resistance to SO_2 than cyanoacrylate glue. The tube is in its turn connected to a high-pressure stainless-steel valve serving as a connection to the pressurization device. It should be noticed that the internal surface of the stainless-steel components in direct contact with SO_2 are treated by Sulfinert® passivation technique. This treatment prevents the active sulfur compounds from reacting with or adsorbing to the metal alloy. Besides pressure that can be controlled using HPOC, it is also possible to control temperature using a heating-cooling stage (Linkam CAP500). Thereby, the gas/water mixtures are analyzed by Raman spectroscopy through the microcapillary at controlled pressure and temperature conditions. Figure 3 shows a simplified sketch of the experimental setup. More details about the installations can be found in Caumon *et al.* and Chou *et al.* [34,39].

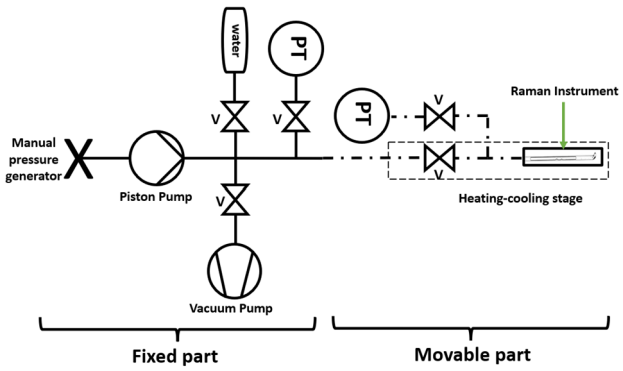

Figure 3: a simplified sketch of the HPOC system coupled with a fused silica capillary set on a heating-cooling stage. The fixed part is composed of a manual pressure generator, pressure transducer (*PT*), valves, and a vacuum pump for purging. The movable part connects the system with the heating-cooling stage.

2.2. Raman Spectroscopy

2.2.1. Calibration process

Raman spectroscopy is able to identify the molecular aspects of the sample based on its characteristic vibrational modes[40]. The spectral features such as peak position, intensity, width, and area depends on molecular structure and physical environment[41].

The quantitative use of Raman spectroscopy is based on the general equation derived from the theory suggested in Placzek *et al.*[40] handbook and detailed in Dhamelincourt *et al.*[42]. The relative

concentrations of two species analyzed at the same time is expressed as follows:

$$\frac{C_A}{C_B} = \frac{A_A/(\sigma_A \times \xi_A)}{A_B/(\sigma_B \times \xi_B)} = \frac{A_A/\sigma_A^*}{A_B/\sigma_B^*} \quad (1)$$

Where A_i is the peak area, C_i the concentration of the species i in the scattering volume, ξ_i the instrumental parameter, σ_i the relative differential scattering cross section (*RDSCS*) of the species, and σ_i^* the effective cross section including the instrumental parameter.

The molar ratio is proportional to the peak area ratio A_A/A_B using the ratio of cross section. However, the value of *RDSCS* for dissolved SO_2 stretching vibration is not available in the literature. Thus, a calibration procedure must be used to relate peak area and concentration. In this work, it is performed by using the solubility data of Rumpf *et al.*[30] (Figure 4), which provide the most complete and coherent set, to calculate the quantification factor (*i.e.* the ratio of the effective cross sections).

In their papers, the authors[30] have studied the solubility of SO_2 in water at temperature values between 20 °C and 120 °C and at pressure lower than 25 bar. The purpose is to determine a relationship between the Peak Area Ratio (*PAR*) and the molality of SO_2 dissolved in water measured by Rumpf *et al.*[30]. The molality is considered as the number of mole of solute per kg of solvent and expressed in mol/kg.

The acquisitions are run at all the *P*,*T* values of the literature data[30] and then at intermediate temperature values (30 °C and 80 °C) in order to better check the reliability of the linear correlation and to provide new solubility data. Raman acquisitions are measured at the exact same pressure of those of literature data[30] using a high precision pressure sensor (± 0.01 bar, type PAA-33X/80794 manufactured by Keller Druck).

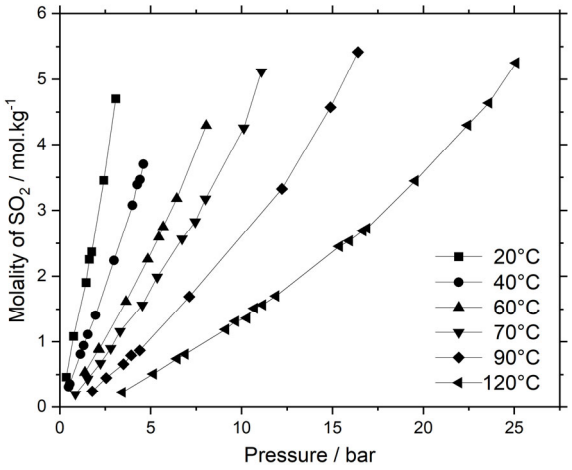

Figure 4: Solubility of SO_2 in water (mol of SO_2 per kg of water) as a function of pressure at different temperature values[30].

The measurement of SO_2 solubility is complex because of its high solubility and because of its type-III phase diagram according to the classification scheme of Van Konynenburg and Scott [43,44]. The measurements are executed from the highest to the lowest targeted pressure to avoid the total dissolution of SO_2 and thus to ensure thermodynamic equilibrium between the liquid and vapor phases.

2.2.2. Raman spectra acquisition

The Raman spectrometer is a LabRAM HR spectrometer (Horiba Jobin-Yvon) equipped with a 1 800 gr.mm^{-1} grating and an Edge filter. The choice behind using a higher groove density is to have higher spectral resolution. The wavelength of the laser is 514.73 nm (Cobolt Fandango). The aperture of the confocal hole is 1 000 µm and a split aperture of 100 µm, focused inside the capillary using a ×20 objective (Olympus). All the spectra are acquired with 6 successive repetitions. Each spectrum was the average of 10 accumulations of 3 s. To have a better accuracy for the peak position and consequently a better determination of the species present, a Neon lamp was placed on the same optical path (Horiba Sample Ref). The lamp provides reference lines for calibrating the peak positions of SO_2 species present in the aqueous solution. Neon peak positions are taken from *NIST* database[45].

The water spectrum consists of a broad O-H stretching vibration[46] band between 3 200 cm^{-1} and 3 400 cm^{-1} and an O-H bending vibration band at 1 650 cm^{-1}. SO_2 has 3 vibrational modes[46]: the deformation mode of O=S=O at ~520 cm^{-1}, the symmetric stretching mode S=O at ~1 150 cm^{-1} and

the asymmetric stretching mode S=O at ~1 320 cm^{-1}. All these modes are Raman active.

The spectra are processed using Laspec6 software (Horiba). A third-order polynomial baseline is first subtracted in the wavenumber interval 800 cm^{-1} – 4 000 cm^{-1}. The peaks are fitted using Gaussian-Lorentzian function. The Raman O-H stretching region is fitted with three Gaussian-Lorentzian sub-bands. The ratio between the area (integrated intensity) of the main SO_2 peak (1 150 cm^{-1}) and the sum of the three peak areas of the stretching band of H_2O is used in this study.

3. Simulation technique

3.1. MC simulation details

Monte Carlo molecular simulations allow to calculate the macroscopic equilibrium properties from a microscopic description of a system using a few hundred to thousand particles. The macroscopic fluid properties are derived by the calculation of averages over some generated microscopic configurations. The GIBBS[47] MC software is used to determine thermodynamic data for SO_2/H_2O mixtures. For this work, the *NPT*-Gibbs ensemble is used to simulate two coexisting phases with a constant total number of particles *N*, a constant pressure *P* and a constant temperature *T*[48]. In the Gibbs ensemble, coexisting phases are simulated by individual simulation boxes without explicit interface. The phase equilibrium is ensured by particle transfers between the two boxes.

Specific MC moves are applied to make the system evolve within the configurational space. Internal Monte Carlo moves (rigid body translations, rigid body rotations, configurational-bias regrowth in case of flexible molecules) are used to impose thermal equilibrium at the considered temperature. Volume changes are used to maintain pressure equilibrium, and molecule transfers between phases allow chemical equilibrium between the two phases. In order to improve the efficiency of the sampling, pre-insertion[49] and orientational[50] biases have been used during the transfer moves of rigid molecules. This algorithm involves two steps. The first step consists in the selection of a suitable location for inserting a new molecule by testing several places with a simple Lennard-Jones particle. The Lennard-Jones parameters used during this step are the parameters of the force field corresponding to the sulfur atom for the SO_2 molecules and to the oxygen atom for the H_2O molecules. Note that the Lennard-Jones particle is not actually inserted. The second step involves the test of several molecular orientations of the true molecule with the center of mass at the location selected in the first step using the Lennard-Jones particle. In this study, we have used 5 trials in the first step and 10 trials in the second step. The acceptance probability of these biased moves is given in references[49] and[50]. For flexible molecules, standard Configurational Bias Monte Carlo (CBMC) has been used[51].

The MC attempt probabilities used for simulations with rigid molecules only are as follow: 0.2975 for translations, 0.2975 for rotations, 0.005 for volume changes and 0.4 for transfers with insertion bias. In case of flexible molecules, the attempt probabilities of the different MC moves are: 0.2 for translations, 0.2 for rotations, 0.2 for configurational-bias regrowth, 0.005 for volume changes and 0.395 for transfers with configurational-bias insertions, The number of MC steps used for equilibration and for production each lies in between 100 and 500 million, one MC step being a single MC move. A total number of 500 water molecules and 50 SO_2 molecules were considered in our MC simulations.

3.2. Force field models

Repulsive-dispersive energy between two *i* and *j* force centers is represented as a function of their separation distance using Lennard-Jones (LJ) potential described in equation (2):

$$U_{ij} = U_{rep} + U_{disp} = 4\varepsilon_{ij}\left(\left(\frac{\sigma_{ij}}{r_{ij}}\right)^{12} - \left(\frac{\sigma_{ij}}{r_{ij}}\right)^{6}\right) \quad (2)$$

where σ and ε represent the LJ parameters. Cross interaction parameters are calculated using Lorentz-Berthelot combining rules. Geometric average for energetic parameters and arithmetic average for diameters are expressed in equations (3) and (4), respectively:

$$\varepsilon_{ij} = \sqrt{\varepsilon_i \varepsilon_j} \quad (3)$$

$$\sigma_{ij} = \frac{\sigma_i + \sigma_j}{2} \quad (4)$$

The Electrostatic energy is computed from the Coulomb law[52]:

$$U_{elec} = \frac{1}{4\pi\varepsilon_0}\frac{q_i q_j}{r_{ij}} \quad (5)$$

where ε_0 is the vacuum permittivity.

Numerous intermolecular potentials have been used to simulate the behavior of fluids involved in CCUS operations, whether pure compounds such as SO_2[32,53–57], N_xO_y[58–61], O_2[55,62,63], N_2[55,62,64] , and Ar[62], or mixtures such as CO_2+SO_2[56,65] , CO_2+O_2[7], CO_2+N_2[7] CO_2+Ar[66], with varying associated performances.

The present study is limited to H_2O and SO_2. Different potential models and their combinations are tested here[53,54,57,67–71] to identify the combination that best agrees with the reference experimental solubility data. The parameters of the considered force fields are reported in Table 1 and

Table ***2*** for SO_2 and H_2O, respectively. For both molecules, we have tested non-polarizable flexible and rigid force fields including localized or delocalized charges. These models have been selected for their precision in reproducing pure compound properties.

Two families of water forcefields were considered: SPC and TIP4P. SPC/E and SPC/Fw are 3-site models[67,68], with three interaction points associated to the three atoms of the water molecules. The oxygen atom is a LJ center plus a negative charge, whereas the two hydrogen atoms carry the positive charges. On the other hand, TIP4P/2005 and TIP4P-Ew[69–71] are intermolecular potentials with 4-sites. In this case, in addition to the three interaction sites located on the three atoms, a negative point charge is placed on the bisector of the $\widehat{HOH}$ angle[32] (represented by M). SPC/Fw[68] is a flexible model, whereas all others are rigid.

Concerning the models applied to SO_2, two models are studied. SO_2(1)[54,56,66] is a rigid 4-site model where the negative charges are located on each oxygen atom and a positive point charge is placed on the bisector of the $\widehat{OSO}$ angle (represented by M) at 0.312 Å from the sulfur atom. SO_2(2)[53] is a flexible 3-site model. In both SO_2 models, in addition to the aforementioned charge distributions, each atom bears a LJ center.

The Lennard-Jones intermolecular energy was computed with a cutoff radius equal to half of the cubic box length, and a classical long-distance correction is applied. According to our simulation conditions, this corresponds to a cutoff value of ~12 Å for the truncation of interactions in the liquid phase. The Ewald summation method is used to calculate long range electrostatic interactions with 7 vectors in each direction of the space and a Gaussian width set to $2\pi/L$, where L is the length of the cubic simulation box.

Table 1: Force field parameters used to model the SO_2 molecule. σ and ε represent the diameter and the energetic parameter of the LJ centers located on the S and O atoms, and q stands for the point charges located on S, O or M centers. k_B is Boltzmann constant.

Model	Force center or charge	σ (Å)	ε/k_B (K)	q (|e|)	d(S-O)	d(S-M)	$\widehat{OSO}$ (°)	Type
SO_2(1)[54]	S	3.5830	126.0800	−	1.434	0.312	119.5	rigid
	O	2.9900	46.4100	-0.4140				
	M(q+)	−	−	0.8280				
SO_2(2)[53,57]	S	3.39	73.8	0.59	1.43	−	119.3	flexible
	O	3.05	79	-0.295				

Table 2: Force field parameters used to model the H_2O molecule. σ and ε represent the diameter and the energetic parameter of the LJ potential located on the oxygen atom and q stands for the point charge located on H atoms for positive charges and on O or M center for negative charges.

Models	Force center or charge	σ (Å)	ε/k_B (K)	q (|e|)	d(O-H)	d(O-M)	$\widehat{HOH}$ (°)	Type
SPC/E[67]	O	3.1655	78.2	-0.8476	1	−	109.47	rigid
	H	−	−	0.4238				
SPC/Fw[68]	O	3.16549	78.2653	-0.82	1.012	−	113.24	flexible
	H	−	−	0.41				
TIP4P/2005[69]	O	3.1589	93.2	−	0.9572	0.1546	104.52	rigid
	H	−	−	0.5564				
	M(q-)		−	-1.1128				
TIP4P-Ew[71]	O	3.16435	81.9	−	0.9572	0.125	104.52	rigid
	H	−	−	0.52422				
	M(q-)			-1.04844				

4. Experimental Results

4.1. SO_2 Raman Spectra

The reactions of SO_2 in water are given in reaction 1 for the first SO_2 dissociation, and in reaction 2 for the second SO_2 dissociation. In water, SO_2 behaves as a weak acid implying that the speciation in solution will be a function of the pH of the solution [72].

$$SO_2 + H_2O \rightleftharpoons HSO_3^- + H^+ \quad pK_a = 1.81 \qquad \text{reaction 1}$$

$$HSO_3^- \rightleftharpoons SO_3^{2-} + H^+ \quad pK_a = 6.97 \qquad \text{reaction 2}$$

During all the measurements done for SO_2/H_2O mixtures, the peak of SO_2 is always present and no SO_3^{2-} is detected as expected knowing the *pKa* (25 °C) of the two dissociation reactions.

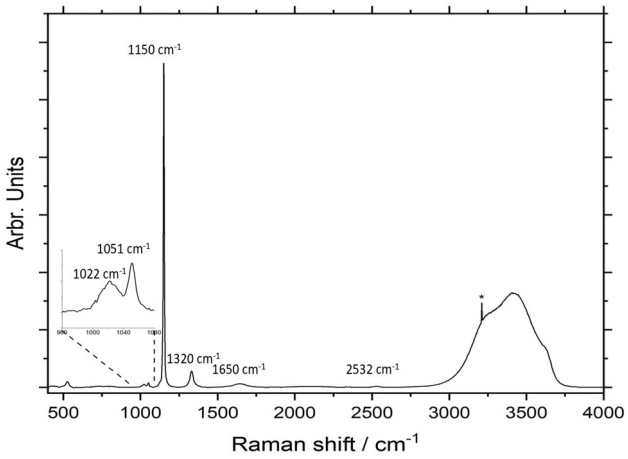

Figure 5: Raman spectrum of SO_2 dissolved in liquid water at 22 °C and 4 bar. * Ne lamp

In Figure 5, we can clearly see a broad series of overlapping bands that are decomposed with Gaussian profiles into two main peaks: 1 022 cm^{-1} and 1 051 cm^{-1}. Previous research proves that HSO_3^- can exist as isomeric forms in aqueous solutions[73–75]. One isomer contains a proton bound to an oxygen atom that can be represented as $(HO)SO_2^-$, and the other isomer contains a proton bound to the sulfur atom represented as $(HS)O_3^-$. An overall equilibrium for isomerization can be written as:

$$(HS)O_3^- \rightleftharpoons (HO)SO_2^- \qquad \text{reaction 3}$$

All the peaks corresponding to these isomers are easily distinguished on the Raman spectrum. The H-S bond is found at 2 532 cm^{-1} and 1 128 cm^{-1} (at 20 °C and 4 bar). The characteristic peak of $(HO)SO_2^-$ isomer is the S-O stretch of H-O-S group at 728 cm^{-1}[75]. The S-O bands at 1 022 cm^{-1} and 1 051 cm^{-1} correspond to $(HO)SO_2^-$ and $(HS)O_3^-$, respectively[76]. It is important to know these reactions because it will help us to determine the solubility of SO_2 based on Raman peak areas. Indeed, Rumpf et *al.*[30] considered two values of solubilities for SO_2. For "true" values, only SO_2 molality are considered. For "overall" values, HSO_3^- and SO_3^{2-} are also considered. For calibrating the Raman data, the "true" values are used as only the main peak of SO_2 is used. Also, in the simulation, the formation of HSO_3^- and SO_3^{2-} are not considered. Besides, some spectra show a sign of oxidation by the presence of SO_4^{2-} by a peak at 980 cm^{-1} [77] corresponding to a limited oxidation of SO_2. The occurrence of an oxidation reaction reduces the solubility values as a part of SO_2 is converted into SO_4^{2-}. Thus, to have an accurate determination of the values, it is essential that no oxidation reaction takes place.

4.2. SO_2 solubility in water

The area of the main SO_2 peak at 1 150 cm^{-1} and the H-O stretching vibration band of water was used to calculate the Peak Area Ratio $A(SO_2)/A(H_2O)$. The *PAR* is plotted as a function of pressure for different temperatures as reported in Figure 6. The slope of the curve combines the *RDSCS* of the SO_2 and H_2O species and the instrument function[42] (equation 1).

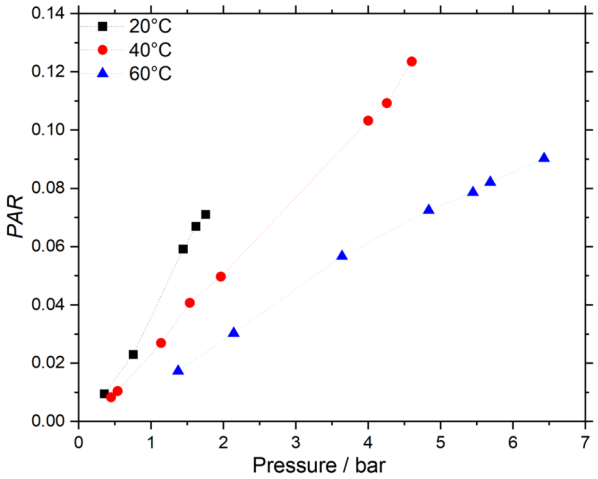

Figure 6: *PAR* as a function of pressure at different temperatures for SO_2 in pure water. Dotted lines are visual guides only.

Using the Raman data and the literature data, it is possible to plot *PAR* as a function of solubility for

each *P*,*T* value (Figure 7). The results show a linear correlation between *PAR* and molality proving the reliability of equation (1).

$$PAR = (0.0319 \pm 0.0005) \times m_{SO_2}\ ,\ R^2 = 0.995 \qquad (6)$$

The determination coefficient R^2 is equal to 0.995. The width of the confidence band does not exceed ± 0.035 in *PAR* scale. The prediction band width is less than ± 0.091 in *PAR* scale. The light dispersion of the points might be due to the experimental uncertainties (*P*,*T*) or also to the appearance of a new phase as the highest pressure represented for each temperature represents the pressure limits before the appearance of a second SO_2-rich liquid phase.

The extrapolation of the range of calibration is possible in the limit of the linearity of the correlation[78]. It is now possible to estimate the solubility at temperatures not provided in literature using equation (6). The measurements of solubility are limited to the liquid-vapor two-phase domain, i.e., before reaching the triphasic line. The concentration of SO_2 injected in the capillary is also a limiting factor: increasing the concentration of SO_2 might lead to a three-phase system including a SO_2-rich liquid phase, a H_2O-rich liquid phase, and a vapor phase or to the liquid-liquid region. On the contrary, reducing the concentration of SO_2 causes the latter to be totally dissolved in water, which leads to a non-linear relationship between *PAR* and pressure because of a loss of chemical equilibrium between the liquid and the gas phases.

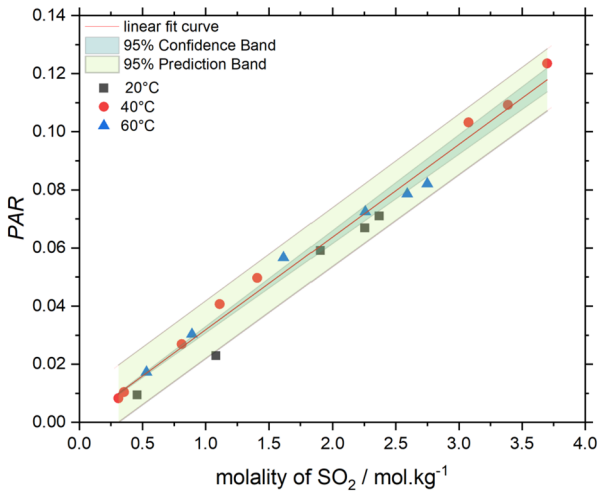

Figure 7: Raman *PAR* as a function of SO_2 solubility[30] in water (mol of SO_2 per kg of water) at different temperatures.

4.3. Effectiveness of *PAR* calibration for other temperatures

The acquisitions of Raman spectra are then run at intermediate temperature values (30 °C and 80 °C) in order to better check the reliability of the linear correlation and to provide new solubility data. Based on equation 6, the experimental data are converted into molar fraction scale at all temperatures in pure water.

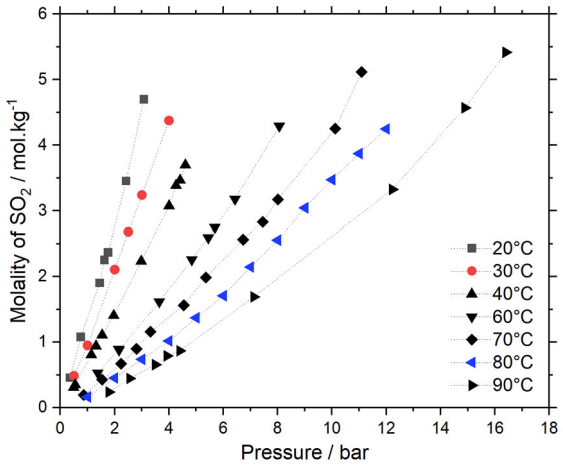

Figure 8: Solubility of SO_2 in water (mol of SO_2 per kg of water) as a function of pressure at different temperatures, including new data at intermediate temperatures of 30 °C and 80 °C. Dotted lines are visual guides only.

Figure 8 represents the solubility of SO_2 in water including the new values at 30 °C and 80 °C. The solubility curves are placed in a coherent order between other temperature values. The new curves show the reliability of the correlation method at intermediate temperatures. Now, SO_2 solubility can be determined using equation 6 for all temperature in the range 30 °C – 80 °C.

5. Monte Carlo simulation results

5.1. Model comparison without binary interaction parameter

Different MC simulations run for SO_2/H_2O mixtures using the models, as previously described in section 3.2, are presented and compared to the experimental data (Figure 9 and Figure 10). A total of 5 combinations of force fields has been evaluated against experimental data of SO_2 solubility in water at 40 °C: SO_2(1)-TIP4P/2005, SO_2(1)-TIP4P-Ew, SO2(1)-SPC/E, SO_2(1)-SPC/Fw, and SO_2(2)-TIP4P/2005. The mixture is always at its vapor-liquid equilibrium. The results show that the combinations SO_2(1)-TIP4P/2005 and SO_2(2)-TIP4P/2005 both underestimate the solubility data. However, using SO_2(2) gives lower solubility data than the values found using the SO_2(1) model. Figure 9 shows the MC simulations run for different water models using SO_2(1) model. The choice of SO_2(1)

force field was dictated by the better accuracy of the results.

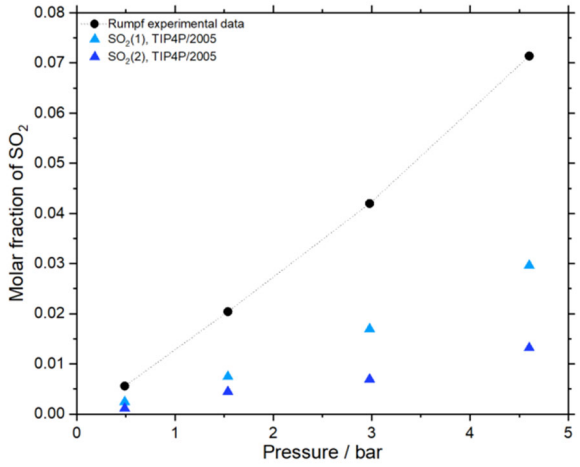

Figure 9: Molecular simulation data of SO_2 solubility in water using different SO_2 and H_2O models at 40 °C. Dotted lines are visual guides only.

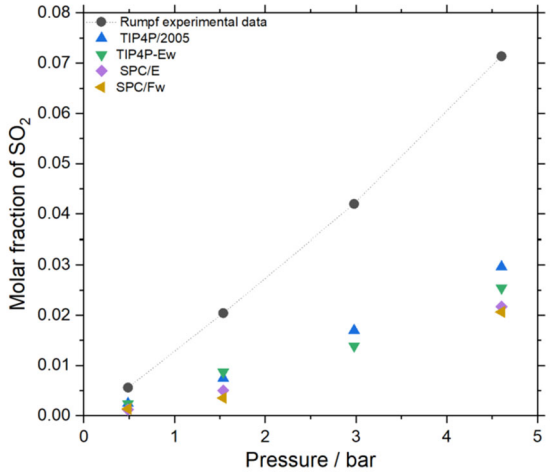

Figure 10: Molecular simulation data of SO_2 solubility in water using different water models at 40 °C (SO_2(1) model is used). Dotted lines are visual guides only.

5.2. Non-zero binary interaction parameter

5.2.1. Temperature-dependent binary interaction parameter

None of the tested model combinations has given a quantitative agreement compared to the experimental data. A possible explanation to this poor quantitative agreement may be related to the use of non-polarizable force fields. Such force fields implicitly account for polarization effects by using adjusted empirical parameters (electrostatic charges and Lennard-Jones parameters). These effective parameters may not be suited for use in other environments, as it is the case when mixtures of different compounds are considered. In order to correct the outcome of the simulation, a binary interaction parameter k_{ij} in the Lorentz-Berthelot mixing rule is introduced. The interaction parameter k_{ij} is introduced to improve the modelling of mixture properties. k_{ij} characterizes the molecular cross interactions between force centers i and j. Introducing the binary interaction parameter has been shown to have a major impact on phase behavior calculations for different applications[79,80]. The dispersive energy parameter is now described as follows instead of equation (3).

$$\varepsilon_{ij} = \sqrt{\varepsilon_i \varepsilon_j}(1 - k_{ij}) \qquad (7)$$

The values of k_{ij}, that can be temperature dependent, can be adjusted to the experimental data of phase equilibria. Here, the k_{ij} values are regressed on experimental solubility data. For each studied temperature, the simulation is run for the highest investigated pressure using different k_{ij} values. The models used for *kij* estimation are SO_2(1) and TIP4P/2005 for SO_2 and H_2O, respectively. Figure 11 shows the error (difference between the simulated and the experimental SO_2 mole fractions) as a function of the k_{ij} value at $T = 40$ °C and $P = 4.6$ bar. The curve intersection with the zero-error value is taken as the optimized k_{ij} parameter for this temperature.

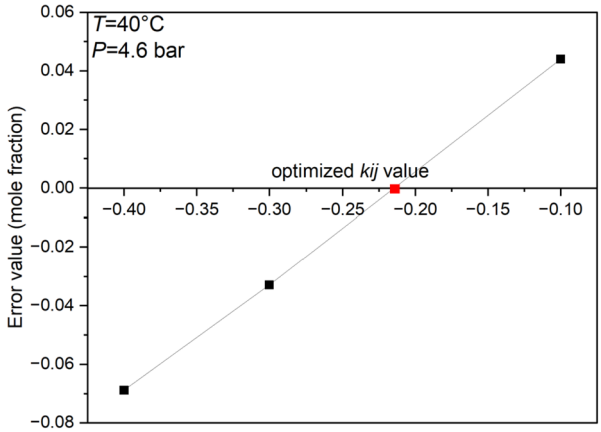

Figure 11: Optimization of the binary interaction parameter at 40 °C. The error value is the difference between the simulated and the experimental SO_2 mole fractions at the studied temperature (40 °C here) and at the highest investigated pressure (4.6 bar here).

Four different temperatures in the range 40 °C – 120 °C have been investigated, leading to the temperature-dependent k_{ij} values plotted in Figure 12. At low temperature, k_{ij} is a decreasing function of temperature. With increasing temperature, the k_{ij} reaches a minimum and then increases. Figure 12 shows that the temperature dependence of the k_{ij} is quadratic.

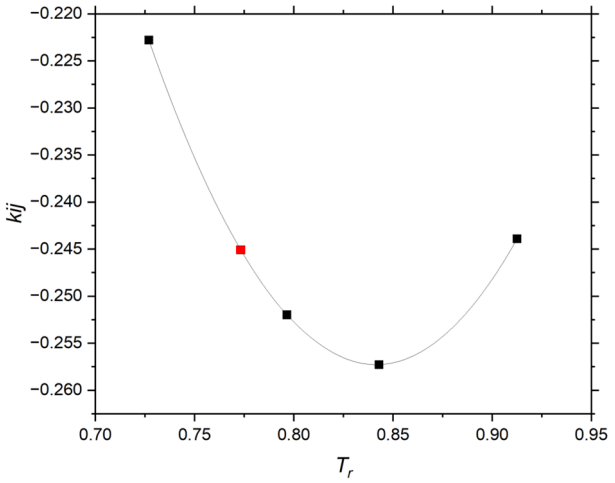

Figure 12: Temperature dependence of the optimized binary interaction parameters (k_{ij}) calculated as a function of the reduced temperature ($Tr = T/T_{C_{SO_2}}$) corresponding to temperatures of 40 °C, 70 °C, 90 °C and 120 °C. The red dot corresponds to the value at 60 °C estimated by the polynomial regression curve.

To check the reliability of the obtained k_{ij} values in predicting solubility data at other temperatures, a simulation was performed at 60 °C using the binary interaction parameter estimated from the curve in Figure 12 (red point). Figure 13 shows that the prediction accuracy of the model is greatly improved by using the optimized binary interaction parameter.

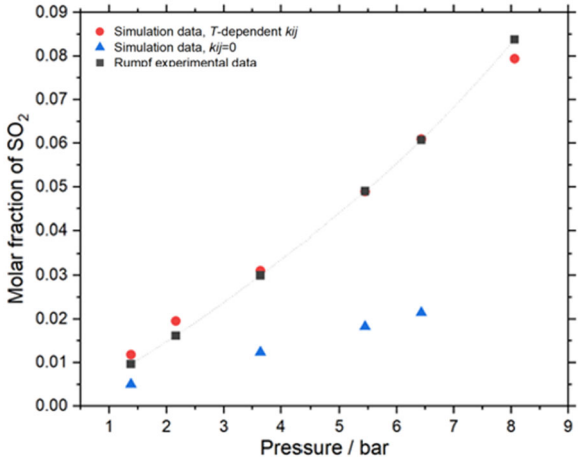

Figure 13: Comparison of simulation data using zero and non-zero binary interaction parameters to the experimental solubility data at 60 °C. The models used for the mixture are SO_2(1) and TIP4P2005 for SO_2 and H_2O, respectively. Dotted lines are visual guides only.

5.2.2. Constant binary interaction parameter

Even if prediction accuracy is improved by using a temperature-dependent k_{ij}, it is a common practice to use a constant binary interaction parameter in a given temperature range in Equation of State modeling. In this section, the possibility of using a constant average value of k_{ij} (k_{ij}=-0.237), independent of temperature, is evaluated for molecular simulation studies. Figure 14 shows that the use of a constant non-zero k_{ij} provides an accurate description of the equilibrium properties of SO_2/H_2O binary mixture.

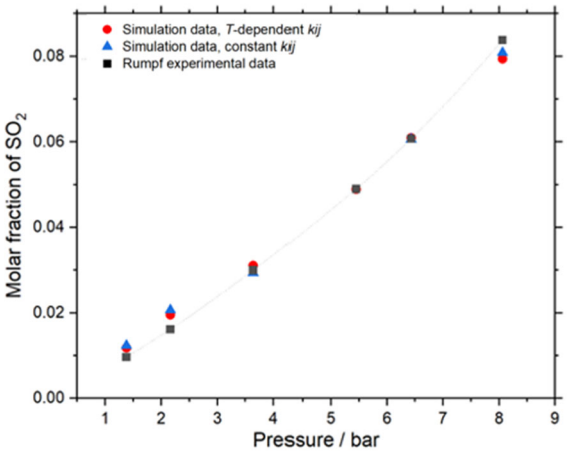

Figure 14: Comparison of simulation data using constant and *T*-dependent binary interaction parameters at 60 °C. The models used for the mixture are SO_2(1) and TIP4P2005 for SO_2 and H_2O, respectively. Dotted lines are visual guides only.

6. Discussion

In the current work, Raman spectroscopy along with literature values and molecular simulation calculations are used to determine the solubility of SO_2 in water. This is relevant to fill the lack of thermodynamic information for fluid mixtures representative of systems encountered in CCUS operations.

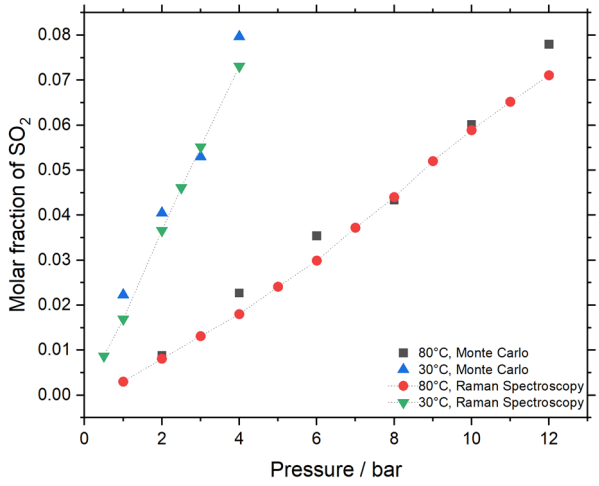

Figure 15: Comparison of solubility data from Raman Spectroscopy and Monte Carlo simulations at 30 °C and 80 °C. The models used for the mixture are SO_2(1) and TIP4P/2005 for SO_2 and H_2O, respectively. Dotted lines are visual guides only.

Figure 15 shows a comparison of Raman data and MC simulation data at 30 °C and 80 °C. The solubility data are not available in all temperatures and pressure values. However, thanks to the equation derived from *PAR* (equation (6), it is possible now to derive new data which can be compared to the MC molecular simulation.

6.1. Experimental challenges

SO_2 is a molecule with high reactivity (redox, acid-base, dismutation, etc.)[19,24]. Some chemical reactions in water were identify using Raman spectroscopy. Despite careful preparation of the samples and evacuation under vacuum before loading gas, oxidation reaction took place in some capillaries, producing SO_4^{2-} ions. Bisulfite ions were also detected in some samples (reaction 1).

Besides, due to the interaction between the previously used cyanoacrylate glue and SO_2, the capillary is glued to the stainless tube using epoxy resin. Indeed, the very first experiments done in the laboratory showed that SO_2 reacted with cyanoacrylate glue which was observed by a quick loss of pressure in the system in less than one hour. The new method shows a good reliability for preventing any gas leak without observed contamination by the glue but the application of the glue on the capillary is more challenging with the epoxy resin than with the cyanoacrylate glue.

The extrapolation from the linearity of the correlation between *PAR* and solubility is possible except for any change of phases or the occurrence of an oxidation reaction and the appearance of sulfates. Therefore, it is necessary to carefully check the phases in equilibrium before and after spectrum acquisition by optical observation and to analyze the spectra during data acquisitions to identify undesired reactions.

6.2. SO_2 solubility in water

Table 3: Molar fraction of SO_2 in water as a function of pressure and temperature from molecular simulation calculations, Raman spectroscopy and Rumpf data[30]. Raman data are given with a standard uncertainty of 1.6%

T / °C	*P* / bar	Molar Fraction		
		Rumpf *et al.* [30]	Raman Spectroscopy	MC
20°C	0.356	0.0083	0.0075	0.014±0.003
	0.756	0.0199	0.0175	–
	1.446	0.0355	0.0324	–
	1.623	0.0423	0.0364	0.046±0.005
	1.758	0.0446	0.0386	–
	2.418	0.0664	0.0548	0.066±0.002
	3.076	0.0925	0.0717	0.094±0.002
30°C	0.5	–	0.0087	–
	1	–	0.0169	0.022±0.002
	2	–	0.0366	0.041±0.003
	2.5	–	0.0461	–
	3	–	0.0552	0.053±0.007
	4	–	0.0731	0.080±0.007
40°C	0.488	0.0056	0.0047	0.0064±0.0001
	0.545	0.0064	0.0059	–
	1.141	0.0148	0.0150	–
	1.314	0.0173	0.0178	–
	1.537	0.0204	0.0225	0.024±0.004
	1.966	0.0260	0.0273	–
	2.979	0.0420	0.0417	0.046±0.008
	4.001	0.0587	0.0551	–
	4.259	0.0650	0.0593	–
	4.409	0.0666	0.0613	–
	4.603	0.0714	0.0672	0.069±0.006
60°C	1.377	0.0097	0.0097	0.012±0.001
	2.143	0.0163	0.0168	0.020±0.002
	2.161	0.0161	0.0172	–
	3.64	0.0300	0.0310	0.031±0.005
	4.838	0.0424	0.0393	–
	5.448	0.0490	0.0425	0.049±0.006
	5.688	0.0521	0.0450	–
	6.43	0.0607	0.0532	0.061±0.009
	8.06	0.0838	0.0705	0.079±0.008
80°C	1	–	0.0030	–
	2	–	0.0081	0.009±0.001
	3	–	0.0131	–
	4	–	0.0180	0.023±0.002
	5	–	0.0241	–
	6	–	0.0299	0.035±0.003
	7	–	0.0372	–
	8	–	0.0440	0.043±0.002
	9	–	0.0520	–
	10	–	0.0589	0.060±0.005
	11	–	0.0652	–
	12	–	0.0711	0.078±0.007

The experimental data points at 40°C are compared with experimental results of different studies [21,23,25,27,28]. The comparison between the experimental values taken from the literature and this work at 40°C shows very good agreement as shown in Figure 16. This agreement demonstrates the suitability of the experimental methodology of the present study for Vapor-Liquid equilibria investigations.

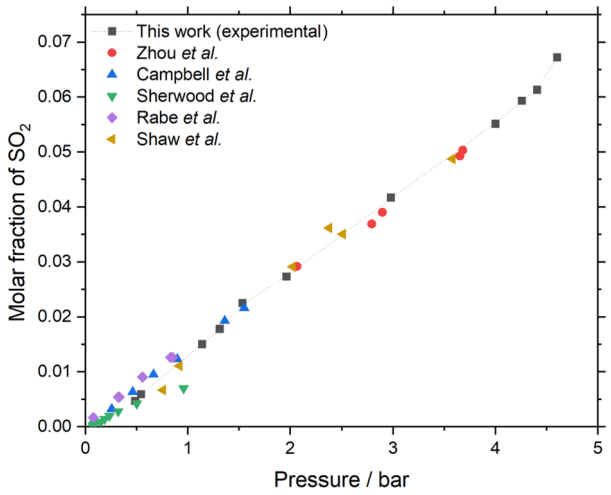

Figure 16: Comparison of values for sulfur dioxide solubility in water at 40°C [21,23,25,27,28]. Dotted lines are visual guides only.

Solubility depends on pressure and temperature. The results show a decrease of solubility when temperature increases and an increase with increasing pressure (Figure 6). The effect of pressure and temperature is similar for some gases such as CO_2 and H_2S. At higher pressures, SO_2 *PAR* (consequently solubility in water) showed a change in slope which is due to the change of phase at higher pressures. The same behavior has been observed for CO_2[81] and H_2S[82].

Raman results and MC simulation showed a better agreement when adding a binary interaction parameter. Temperature-dependent and constant k_{ij} values showed as good results for the whole studied *P*,*T* range. This demonstrates the transferability of the parameterization under the investigated conditions.

6.3. Liquid-Liquid phase

To study the phase composition of the liquid-liquid SO_2/H_2O binary system, we propose the use of the binary interaction parameter previously determined for this system at lower pressure conditions where vapor-liquid equilibrium occurs. Previous molecular simulation studies were already conducted in the liquid-liquid domain without the use of binary interaction parameters[32]. However, the obtained SO_2 content of the water-rich branch of the liquid-liquid domain was slightly underestimated by molecular simulations compared to the experimental values[83]. The combination of SO_2(1)/TIP4P/2005 was used as well for studying the liquid-liquid phase.

In a first step, only a constant binary parameter (k_{ij}=-0.237) is used. The results are shown in Table 4 where L1 stands for H_2O-rich liquid. Using a constant binary interaction parameter shows better results in the liquid-liquid region for the solubility of SO_2 in the H_2O-rich phase compared to the simulations run without introducing k_{ij} values[32].

Table 4: Phase composition for the SO_2+H_2O binary systems at 50 °C where L1stands for the liquid H_2O-rich phase.

Pressure/ bar	Molar fraction of SO_2	
	Sayegh et *al.*[83]	MC k_{ij}=-0.237
	L1	L1
30	0.068	0.091±0.006
50	0.070	0.084±0.004

7. Conclusion

To ensure the long-term CO_2 storage under safe and sustainable conditions, it is mandatory to take the co-injected gases into consideration when designing and processing the capture, transport, and storage. New solubility data for SO_2 were provided using the linear relationship between Raman and literature data. The solubility of SO_2 in water was also investigated by means of molecular simulation techniques, which have been proven as valuable complementary approaches to experimental measurements. The new calibration of vapor-liquid data using binary interaction parameters showed a good agreement with the experimental data. The new data of solubility in aqueous solutions can be used to fit equations of state and to implement the geochemical codes used to simulate water/gas/rock interactions in the case of the geological storage of CO_2 with SO_2. FSCC technique appears as a suitable technique to fill the lack of information. The experimental device will be used in further studies to measure the solubility of gas mixtures containing CO_2 and annex gases such as NO, H_2S or SO_2, controlling phase transitions by optical microscopic observations as well as chemical speciation and equilibria by Raman spectroscopy.

Acknowledgement

This work was partially supported by INSU CESSUR grant and Carnot Icéel grant (FOMICRO). A special acknowledgement goes to IFPEN and the University of Paris-Saclay for providing the GIBBS MC code. High Performance Computing resources were partially supplied by the EXPLOR centre hosted by the University of Lorraine.

References

[1] IPCC, ed., Framing and Context, in: Global Warming of 1.5°C: IPCC Special Report on Impacts of Global Warming of 1.5°C above Pre-Industrial Levels in Context of Strengthening Response to Climate Change, Sustainable Development, and Efforts to Eradicate Poverty, Cambridge University Press, Cambridge, 2022: pp. 49–92. https://doi.org/10.1017/9781009157940.003.

[2] R.A. Berner, The long-term carbon cycle, fossil fuels and atmospheric composition, Nature. 426 (2003) 323–326. https://doi.org/10.1038/nature02131.

[3] A. Torvanger, M.T. Lund, N. Rive, Carbon capture and storage deployment rates: needs and feasibility, Mitig Adapt Strateg Glob Change. 18 (2013) 187–205. https://doi.org/10.1007/s11027-012-9357-7.

[4] S. Thibeau, P. Chiquet, G. Mouronval, M. Lescanne, Geochemical assessment of the injection of CO2 into Rousse depleted gas reservoir, Energy Procedia. 1 (2009) 3383–3390. https://doi.org/10.1016/j.egypro.2009.02.127.

[5] M. Anheden, J. Yan, G.D. Smedt, Denitrogenation (or Oxyfuel Concepts), Oil & Gas Science and Technology - Rev.IFP. 60 (2005) 485–495. https://doi.org/10.2516/ogst:2005030.

[6] J. Wang, D. Ryan, E.J. Anthony, A. Wigston, L. Basava-Reddi, N. Wildgust, The effect of impurities in oxyfuel flue gas on CO2 storage capacity, International Journal of Greenhouse Gas Control. 11 (2012) 158–162. https://doi.org/10.1016/j.ijggc.2012.08.002.

[7] B. Creton, T. de Bruin, D. Le Roux, P. Duchet-Suchaux, V. Lachet, Impact of Associated Gases on Equilibrium and Transport Properties of a CO2 Stream: Molecular Simulation and Experimental Studies, Int. J. Thermophys. 35 (2014) 256–276. https://doi.org/10.1007/s10765-014-1592-6.

[8] J. Sterpenich, J. Dubessy, J. Pironon, S. Renard, M.-C. Caumon, A. Randi, J.-N. Jaubert, E. Favre, D. Roizard, M. Parmentier, M. Azaroual, V. Lachet, B. Creton, T. Parra, E. El Ahmar, C. Coquelet, V. Lagneau, J. Corvisier, P. Chiquet, Role of Impurities on CO2 Injection: Experimental and Numerical Simulations of Thermodynamic Properties of Water-salt-gas Mixtures (CO2 + Co-injected Gases) Under Geological Storage Conditions, Energy Procedia. (2013) pp.3638-3645. https://doi.org/10.1016/j.egypro.2013.06.257.

[9] B. Metz, O. Davidson, H.C. De Coninck, M. Loos, L. Meyer, IPCC special report on carbon dioxide capture and storage, Cambridge: Cambridge University Press, 2005.

[10] J. Corvisier, I. Sin, Considering Non-Ideal Gas Mixtures in Geochemical Modeling of Gas-Water-Salt-Rock Interactions: Application to Impure CO2 Geological Storage, (2019). https://doi.org/10.2139/ssrn.3365754.

[11] D.-Y. Peng, D.B. Robinson, A New Two-Constant Equation of State, Ind. Eng. Chem. Fundamen. 15 (1976) 59–64. https://doi.org/10.1021/i160057a011.

[12] H. Li, J. Yan, J. Yan, M. Anheden, Impurity impacts on the purification process in oxy-fuel combustion based CO2 capture and storage system, Applied Energy. 86 (2009) 202–213. https://doi.org/10.1016/j.apenergy.2008.05.006.

[13] Gas Encyclopedia | Gas Encyclopedia Air Liquide, (n.d.). https://encyclopedia.airliquide.com/gas-encyclopedia (accessed May 1, 2023).

[14] W.L. Beuschlein, L.O. Simenson, Solubility of Sulfur Dioxide in Water, J. Am. Chem. Soc. 62 (1940) 610–612. https://doi.org/10.1021/ja01860a053.

[15] J.J. Byerley, G.L. Rempel, V.T. Le, Solubility of sulfur dioxide in water-acetonitrile solutions, J. Chem. Eng. Data. 25 (1980) 55–56. https://doi.org/10.1021/je60084a017.

[16] F.H. Conrad, W.L. Beuschlein, Some Equilibrium Relations in the System Calcium Oxide—Sulfur Dioxide—Water (Acid Region) at Pressures below Atmospheric1, J. Am. Chem. Soc. 56 (1934) 2554–2562. https://doi.org/10.1021/ja01327a009.

[17] J.C. Hudson, CLXXXIII.—The solubility of sulphur dioxide in water and in aqueous solutions of potassium chloride and sodium sulphate, J. Chem. Soc., Trans. 127 (1925)

1332–1347. https://doi.org/10.1039/CT9252701332.
[18] C.E. Maass, O. Maass, SULFUR DIOXIDE AND ITS AQUEOUS SOLUTIONS. I. ANALYTICAL METHODS, VAPOR DENSITY AND VAPOR PRESSURE OF SULFUR DIOXIDE. VAPOR PRESSURE AND CONCENTRATIONS OF THE SOLUTIONS, J. Am. Chem. Soc. 50 (1928) 1352–1368. https://doi.org/10.1021/ja01392a016.
[19] M.K. Mondal, Experimental determination of dissociation constant, Henry's constant, heat of reactions, SO2 absorbed and gas bubble–liquid interfacial area for dilute sulphur dioxide absorption into water, Fluid Phase Equilib. 253 (2007) 98–107. https://doi.org/10.1016/j.fluid.2007.01.015.
[20] Wm.T. Smith, R.B. Parkhurst, THE SOLUBILITY OF SULFUR DIOXIDE IN SUSPENSIONS OF CALCIUM AND MAGNESIUM HYDROXIDES, J. Am. Chem. Soc. 44 (1922) 1918–1927. https://doi.org/10.1021/ja01430a010.
[21] T.K. Sherwood, Solubilities of Sulfur Dioxide and Ammonia in Water., Ind. Eng. Chem. 17 (1925) 745–747. https://doi.org/10.1021/ie50187a043.
[22] H.F. Johnstone, P.W. Leppla, The Solubility of Sulfur Dioxide at Low Partial Pressures. The Ionization Constant and Heat of Ionization of Sulfurous Acid1, J. Am. Chem. Soc. 56 (1934) 2233–2238. https://doi.org/10.1021/ja01326a009.
[23] A.E. Rabe, J.F. Harris, Vapor Liquid Equilibrium Data for the Binary System Sulfur Dioxide and Water., J. Chem. Eng. Data. 8 (1963) 333–336. https://doi.org/10.1021/je60018a017.
[24] M.A. Siddiqi, J. Krissmann, P. Peters-Gerth, M. Luckas, K. Lucas, Spectrophotometric measurement of the vapour-liquid equilibria of (sulphur dioxide + water), J. Chem. Thermodyn. 28 (1996) 685–700. https://doi.org/10.1006/jcht.1996.0064.
[25] Q. Zhou, H. Guo, P. Yang, Z. Wang, Solubility of SO2 in Water from 263.15 to 393.15 K and from 10 to 300 bar: Quantitative Raman Spectroscopic Measurements and PC-SAFT Prediction, Industrial & Engineering Chemistry Research. 59 (2020) 12855–12861. https://doi.org/10.1021/acs.iecr.9b06242.
[26] H.W.B. Roozeboom, Sur l'hydrate de l'acide sulfureux, Recueil Des Travaux Chimiques Des Pays-Bas. 3 (1884) 29–58. https://doi.org/10.1002/recl.18840030202.
[27] P. Cui, T.-T. Wang, Q. Wang, B. Li, Measurements of vapor-liquid equilibrium data of sulfur dioxide-1,4-bis (2-hydroxypropyl) piperazine sulfate aqueous solutions, Gao Xiao Hua Xue Gong Cheng Xue Bao/Journal of Chemical Engineering of Chinese Universities. 28 (2014) 454–459. https://doi.org/10.3969/j.issn.1003-9015.2014.03.003.
[28] W.B. Campbell, O. Maass, Equilibria in sulphur dioxide solutions, Can. J. Res. 2 (1930) 42–64. https://doi.org/10.1139/cjr30-006.
[29] J. Lindner, Die elektrolytische Dissoziation der schwefligen Säure, Monatshefte für Chemie. 33 (1912) 613–672. https://doi.org/10.1007/BF01519312.
[30] B. Rumpf, G. Maurer, Solubilities of hydrogen cyanide and sulfur dioxide in water at temperatures from 293.15 to 413.15 K and pressures up to 2.5 MPa, Fluid Phase Equilibria. 81 (1992) 241–260. https://doi.org/10.1016/0378-3812(92)85155-2.
[31] Dioxyde de soufre (FT 41). Généralités - Fiche toxicologique - INRS, (n.d.). https://www.inrs.fr/publications/bdd/fichetox/fiche.html?refINRS=FICHETOX_41 (accessed June 21, 2022).
[32] B. Creton, C. Nieto-Draghi, T. de Bruin, V. Lachet, E. El Ahmar, A. Valtz, C. Coquelet, S. Lasala, R. Privat, J.-N. Jaubert, Thermodynamic study of binary systems containing sulphur dioxide and nitric oxide: Measurements and modelling, Fluid Phase Equilib. 461 (2018) 84–100. https://doi.org/10.1016/j.fluid.2017.12.036.
[33] Q. Hu, H. Guo, X. Lü, W. Lu, Y. Chen, Y. Zhu, L. Geng, Determination of P–V–T–x properties of the CO2–H2O system up to 573.15K and 120MPa—Experiments and model, Chem. Geol. 424 (2016) 60–72. https://doi.org/10.1016/j.chemgeo.2016.01.011.
[34] M.-C. Caumon, J. Dubessy, P. Robert, A. Tarantola, Fused-silica capillary capsules (FSCCs) as reference synthetic aqueous fluid inclusions to determine chlorinity by Raman spectroscopy, Eur. J. Mineral. 25 (2014) 755–763. https://doi.org/10.1127/0935-1221/2013/0025-2280.
[35] Q. Hu, X. Lü, W. Lu, Y. Chen, H. Liu, An extensive study on Raman spectra of water from 253 to 753K at 30MPa: A new insight into structure of water, J. Mol. Spectrosc. 292 (2013) 23–27. https://doi.org/10.1016/j.jms.2013.09.006.

[36] W. Lu, H. Guo, I.M. Chou, R.C. Burruss, L. Li, Determination of diffusion coefficients of carbon dioxide in water between 268 and 473K in a high-pressure capillary optical cell with in situ Raman spectroscopic measurements, Geochim. Cosmochim. Acta. 115 (2013) 183–204. https://doi.org/10.1016/j.gca.2013.04.010.

[37] M.-C. Caumon, J. Dubessy, P. Robert, B. Benaissa, Microreactors to Measure Solubilities in the CO2-H2O-NaCl System, Energy Procedia. 114 (2017) 4843–4850. https://doi.org/10.1016/j.egypro.2017.03.1624.

[38] I.-M. Chou, R.C. Burruss, W. Lu, Chapter 24 - A new optical capillary cell for spectroscopic studies of geologic fluids at pressures up to 100 MPa, in: J. Chen, Y. Wang, T.S. Duffy, G. Shen, L.F. Dobrzhinetskaya (Eds.), Advances in High-Pressure Technology for Geophysical Applications, Elsevier, Amsterdam, 2005: pp. 475–485. https://doi.org/10.1016/B978-044451979-5.50026-0.

[39] I.-M. Chou, Y. Song, R.C. Burruss, A new method for synthesizing fluid inclusions in fused silica capillaries containing organic and inorganic material, Geochim. Cosmochim. Acta. 72 (2008) 5217–5231. https://doi.org/10.1016/j.gca.2008.07.030.

[40] G. Placzek, The Rayleigh and Raman scattering, Lawrence Radiation Laboratory, Berkeley, Calif, 1959.

[41] R.E. Connick, T.M. Tam, E. Von Deuster, Equilibrium constant for the dimerization of bisulfite ion to form disulfite(2-) ion, Inorg. Chem. 21 (1982) 103–107. https://doi.org/10.1021/ic00131a020.

[42] N. Guilhaumou, P. Dhamelincourt, J.-C. Touray, J. Touret, Etude des inclusions fluides du système N2-CO2 de dolomites et de quartz de Tunisie septentrionale. Données de la microcryoscopie et de l'analyse à la microsonde à effet Raman, Geochim. Cosmochim. Acta. 45 (1981) 657–673. https://doi.org/10.1016/0016-7037(81)90040-5.

[43] R. Privat, J.-N. Jaubert, Classification of global fluid-phase equilibrium behaviors in binary systems, Chem. Eng. Res. Des. 91 (2013) 1807–1839. https://doi.org/10.1016/j.cherd.2013.06.026.

[44] P.H. van Konynenburg, R.L. Scott, J.S. Rowlinson, Critical lines and phase equilibria in binary van der Waals mixtures, Philosophical Transactions of the Royal Society of London. Series A, Mathematical and Physical Sciences. 298 (1980) 495–540. https://doi.org/10.1098/rsta.1980.0266.

[45] curtis.suplee@nist.gov, Atomic Spectra Database, NIST. (2009). https://www.nist.gov/pml/atomic-spectra-database (accessed June 7, 2022).

[46] T. Shimanouchi, H. Matsuura, Y. Ogawa, I. Harada, Tables of molecular vibrational frequencies, J. Phys. Chem. Ref. Data. 7 (1978) 1323–1444. https://doi.org/10.1063/1.555587.

[47] P. Ungerer, V. Lachet, B. Tavitian, Applications of Molecular Simulation in Oil and Gas Production and Processing, Oil & Gas Science and Technology - Rev. IFP. 61 (2006) 387–403. https://doi.org/10.2516/ogst:2006040a.

[48] A.Z. Panagiotopoulos, N. Quirke, M. Stapleton, D.J. Tildesley, Phase equilibria by simulation in the Gibbs ensemble - Alternative derivation, generalization and application to mixture and membrane equilibria, Molecular Physics. 63 (1988) 527–545. https://doi.org/10.1080/00268978800100361.

[49] E. Bourasseau, P. Ungerer, A. Boutin, Prediction of Equilibrium Properties of Cyclic Alkanes by Monte Carlo SimulationNew Anisotropic United Atoms Intermolecular PotentialNew Transfer Bias Method, J. Phys. Chem. B. 106 (2002) 5483–5491. https://doi.org/10.1021/jp014190r.

[50] V. Lachet, A. Boutin, B. Tavitian, A.H. Fuchs, Computational Study of p-Xylene/m-Xylene Mixtures Adsorbed in NaY Zeolite, J. Phys. Chem. B. 102 (1998) 9224–9233. https://doi.org/10.1021/jp980946j.

[51] B. Smit, S. Karaborni, J.I. Siepmann, Computer simulations of vapor–liquid phase equilibria of n-alkanes, The Journal of Chemical Physics. 102 (1995) 2126–2140. https://doi.org/10.1063/1.469563.

[52] J.-C. Neyt, A. Wender, V. Lachet, P. Malfreyt, Prediction of the Temperature Dependence of the Surface Tension Of SO_2, N_2, O_2, and Ar by Monte Carlo Molecular Simulations, J. Phys. Chem. B. 115 (2011) 9421–9430. https://doi.org/10.1021/jp204056d.

[53] G. Kamath, M. Ketko, G.A. Baker, J.J. Potoff, Monte Carlo predictions of phase equilibria and structure for dimethyl ether + sulfur dioxide and dimethyl ether + carbon dioxide, J. Chem. Phys. 136 (2012) 044514. https://doi.org/10.1063/1.3677880.

[54] E. El Ahmar, B. Creton, A. Valtz, C. Coquelet, V. Lachet, D. Richon, P. Ungerer, Thermodynamic study of binary systems containing sulphur dioxide: Measurements and molecular modelling, Fluid Phase Equilib. 304 (2011) 21–34. https://doi.org/10.1016/j.fluid.2011.02.008.

[55] J. Yang, Y. Ren, A. Tian, H. Sun, COMPASS Force Field for 14 Inorganic Molecules, He, Ne, Ar, Kr, Xe, H2, O2, N2, NO, CO, CO2, NO2, CS2, and SO2, in Liquid Phases, J. Phys. Chem. B. 104 (2000) 4951–4957. https://doi.org/10.1021/jp992913p.

[56] X. Xu, R. Privat, J.-N. Jaubert, V. Lachet, B. Creton, Phase equilibrium of CCS mixtures: Equation of state modeling and Monte Carlo simulation, J. Supercrit. 119 (2017) 169–202. https://doi.org/10.1016/j.supflu.2016.09.013.

[57] M.H. Ketko, G. Kamath, J.J. Potoff, Development of an optimized intermolecular potential for sulfur dioxide, J Phys Chem B. 115 (2011) 4949–4954. https://doi.org/10.1021/jp2010524.

[58] V. Lachet, B. Creton, T. de Bruin, E. Bourasseau, N. Desbiens, Ø. Wilhelmsen, M. Hammer, Equilibrium and transport properties of CO2+N2O and CO2+NO mixtures: Molecular simulation and equation of state modelling study, Fluid Phase Equilibria. 322–323 (2012) 66–78. https://doi.org/10.1016/j.fluid.2012.03.011.

[59] J.O. Hirschfelder, C.F. Curtiss, R.B. Bird, Molecular Theory of Gases and Liquids, Physics Today. 8 (1955) 17. https://doi.org/10.1063/1.3061949.

[60] F. Kohler, M. Bohn, J. Fischer, R. Zimmermann, The excess properties of nitric oxid mixtures, Monatsh Chem. 118 (1987) 169–182. https://doi.org/10.1007/BF00810050.

[61] M.F. Costa Gomes, J. Deschamps, A.A.H. Pádua, Interactions of Nitrous Oxide with Fluorinated Liquids, J. Phys. Chem. B. 110 (2006) 18566–18572. https://doi.org/10.1021/jp062995z.

[62] J. Vrabec, J. Stoll, H. Hasse, A Set of Molecular Models for Symmetric Quadrupolar Fluids, J. Phys. Chem. B. 105 (2001) 12126–12133. https://doi.org/10.1021/jp012542o.

[63] Y. Boutard, Ph. Ungerer, J.M. Teuler, M.G. Ahunbay, S.F. Sabater, J. Pérez-Pellitero, A.D. Mackie, E. Bourasseau, Extension of the anisotropic united atoms intermolecular potential to amines, amides and alkanols: Application to the problems of the 2004 Fluid Simulation Challenge, Fluid Phase Equilibria. 236 (2005) 25–41. https://doi.org/10.1016/j.fluid.2005.06.009.

[64] J. DELHOMMELLE, Etablissement de potentiels d'interaction pour la simulation moleculaire. Application a la prediction des equilibres liquide-vapeur de melanges binaires alcane-molecule multipolaire, These de doctorat, Paris 11, 2000. https://theses.fr/2000PA112024 (accessed June 19, 2023).

[65] V. Lachet, T. de Bruin, P. Ungerer, C. Coquelet, A. Valtz, V. Hasanov, F. Lockwood, D. Richon, Thermodynamic behavior of the CO2+SO2 mixture: Experimental and Monte Carlo simulation studies, Energy Procedia. 1 (2009) 1641–1647. https://doi.org/10.1016/j.egypro.2009.01.215.

[66] B. Creton, V. Lachet, Thermodynamic Study of Binary Systems Containing Carbon Dioxide and Associated Gases Using Molecular Simulation Techniques, SSRN Journal. (2019). https://doi.org/10.2139/ssrn.3365730.

[67] H.J.C. Berendsen, J.R. Grigera, T.P. Straatsma, The missing term in effective pair potentials, J. Phys. Chem. 91 (1987) 6269–6271. https://doi.org/10.1021/j100308a038.

[68] Y. Wu, H.L. Tepper, G.A. Voth, Flexible simple point-charge water model with improved liquid-state properties, J. Chem. Phys. 124 (2006) 024503. https://doi.org/10.1063/1.2136877.

[69] J.L.F. Abascal, C. Vega, A general purpose model for the condensed phases of water: TIP4P/2005, The Journal of Chemical Physics. 123 (2005) 234505-234505–12. https://doi.org/10.1063/1.2121687.

[70] W.L. Jorgensen, J. Chandrasekhar, J.D. Madura, R.W. Impey, M.L. Klein, Comparison of simple potential functions for simulating liquid water, J. Chem. Phys. 79 (1983) 926–935. https://doi.org/10.1063/1.445869.

[71] H.W. Horn, W.C. Swope, J.W. Pitera, J.D. Madura, T.J. Dick, G.L. Hura, T. Head-Gordon, Development of an improved four-site water model for biomolecular simulations: TIP4P-Ew, J. Chem. Phys. 120 (2004) 9665–9678. https://doi.org/10.1063/1.1683075.

[72] E. Damian Risberg, L. Eriksson, J. Mink, L.G.M. Pettersson, M.Yu. Skripkin, M. Sandström, Sulfur X-ray Absorption and Vibrational Spectroscopic Study of Sulfur Dioxide, Sulfite, and Sulfonate Solutions and of the Substituted Sulfonate Ions $X_3CSO_3^-$ (X = H, Cl, F), Inorg.

Chem. 46 (2007) 8332–8348. https://doi.org/10.1021/ic062440i.
[73] D.A. Horner, R.E. Connick, Equilibrium quotient for the isomerization of bisulfite ion from HSO3- to SO3H-, Inorg. Chem. 25 (1986) 2414–2417. https://doi.org/10.1021/ic00234a026.
[74] D.A. Horner, R.E. Connick, Kinetics of Oxygen Exchange between the Two Isomers of Bisulfite Ion, Disulfite Ion ($S_2O_5^{2-}$), and Water As Studied by Oxygen-17 Nuclear Magnetic Resonance Spectroscopy, Inorg. Chem. 42 (2003) 1884–1894. https://doi.org/10.1021/ic020692n.
[75] A. Simon, H. Kriegsmann, Zu den Ionengleichgewichten in den wäßrigen Lösungen der sauren Sulfite, Chemische Berichte. 89 (1956) 2442–2446. https://doi.org/10.1002/cber.19560891037.
[76] D. Littlejohn, S.A. Walton, S.-G. Chang, A Raman Study of the Isomers and Dimer of Hydrogen Sulfite Ion, Appl Spectrosc. 46 (1992) 848–851. https://doi.org/10.1366/0003702924124592.
[77] B. Meyer, M. Ospina, L.B. Peter, Raman spectrometric determination of oxysulfur anions in aqueous systems, Anal. Chim. Acta. 117 (1980) 301–311. https://doi.org/10.1016/0003-2670(80)87030-9.
[78] J. Sterpenich, M. Caumon, V. Lachet, B. Creton, M. El Jarmouni, A. Randi, P. Robert, NO solubility in water and brine up to 60 MPa and 373 K by combining Raman spectroscopy and molecular simulation, J. Raman Spectrosc. 53 (2022) 645–653. https://doi.org/10.1002/jrs.6072.
[79] R. Fauve, X. Guichet, V. Lachet, N. Ferrando, Prediction of H2S solubility in aqueous NaCl solutions by molecular simulation, J. Pet. Sci. Eng. 157 (2017) 94–106. https://doi.org/10.1016/j.petrol.2017.07.003.
[80] Y. Liu, A.Z. Panagiotopoulos, P.G. Debenedetti, Monte Carlo Simulations of High-Pressure Phase Equilibria of CO_2–H_2O Mixtures, J. Phys. Chem. B. 115 (2011) 6629–6635. https://doi.org/10.1021/jp201520u.
[81] M.-C. Caumon, J. Sterpenich, A. Randi, J. Pironon, Measuring mutual solubility in the H2O–CO2 system up to 200 bar and 100 °C by in situ Raman spectroscopy, International Journal of Greenhouse Gas Control. 47 (2016) 63–70. https://doi.org/10.1016/j.ijggc.2016.01.034.
[82] Z. Duan, R. Sun, R. Liu, C. Zhu, Accurate Thermodynamic Model for the Calculation of H2S Solubility in Pure Water and Brines, Energy Fuels. 21 (2007) 2056–2065. https://doi.org/10.1021/ef070040p.
[83] S.G. Sayegh, J. Najman, Phase behavior measurements of CO2-SO2-brine mixtures, Can. J. Chem. Eng. 65 (1987) 314–320. https://doi.org/10.1002/cjce.5450650218.